Korean J. Chem. Eng., 34(5), 1563-1575 (2017)
DOI: 10.1007/s11814-017-0001-9

pISSN: 0256-1115
eISSN: 1975-7220

Experimental and numerical predictions of ash particle erosion in SCR monolithic catalysts for coal-fired utility boilers

Cong Yu*, Fengqi Si*,†, Shaojun Ren*, and Xiaoming Jiang**

*School of Energy and Environment, Southeast University, Nanjing 210096, P. R. China
**Datang Nanjing Environmental Protection Technology Co., Ltd., Nanjing 211111, P. R. China
(*Received 14 July 2016 • accepted 1 January 2017*)

Abstract−Erosion by particles in monolithic selective catalyst reduction (SCR) processes can reduce the operational life of a catalyst and threaten the performance of the SCR system. We present an integrated approach implemented in two stages to predict the erosion condition of SCR processes. First, a 3D computational fluid dynamics (CFD) model was established for a full-sized SCR reactor to obtain information on the flue gas and ash particles at the entrance of the catalyst layer. Second, the detailed inner catalyst structure layers were simulated using MATLAB and a catalyst erosion model was developed, according to the initial and boundary conditions obtained using the CFD models. Relative cold state tests and erosion measurements were conducted to validate the simulation results. The model was applied to investigate the relationship between the reactor installment, the gas-solid flow field and the catalyst erosion. Moreover, a series of retrofit schemes were implemented to confirm that this method can be used in engineering applications.

Keywords: Coal-fired Boiler, SCR Catalysts, Ash Particle Erosion, CFD, Coupling Calculation

INTRODUCTION

Nitrogen oxide (NOx) is a major air pollutant released from coal-fired utility boilers that has raised considerable concern among environmental agencies. The selective catalytic reduction (SCR) process is an effective and widely applied technology in which the reagent (ammonia or urea) can selectively react with NOx and transform NOx into harmless water and nitrogen on the surface of the catalyst. In coal-fired plants, SCR DeNOx systems are commonly installed in high-dust (HD) environments between the economizer and the air preheater because of the optimal temperature for catalyst activity in this region [1]. However, the removal of fly ash particles via an electrostatic precipitator (ESP) is not accomplished in an HD configuration; therefore, massive quantities of ash articles generated from coal combustion [2] can pass through the SCR catalysts and significantly promote catalyst deactivation via chemical poisoning, blinding or plugging of the catalyst passages [3,4].

Ash particle erosion is another major issue that promotes catalyst deactivation and may reduce the active components of the catalytic material [5]. For SCR monolithic catalysts, the reaction occurs inside the pore structure of the catalyst instead of at the surface; thus, the coating thickness of the catalytic material affects the catalytic activity [6-8]. Yang et al. [9] determined that NO conversion decreases remarkably with a decrease in the coating thickness from 90 μm to 50 μm, whereas the variation of the conversion rate decreases to a much lesser degree at thicknesses greater than 90 μm. This finding indicates that the catalyst erosion caused by ash particles, which may induce local severe damage, is a threat to the performance of SCR systems and may require early catalyst regeneration and replacement to meet emissions constraints, thereby leading to unwanted unit shutdowns and added costs in terms of lost production and catalyst service life [10,11]. Therefore, an integrated method for performing catalyst erosion analyses is desired to predict the erosion rate and the position at which severe erosion is more likely to occur.

Currently, a limited number of studies have focused on predicting erosion in SCR monolithic catalysts in coal-fired utility boilers. Theoretically, most of the erosion models are concentrated on metal materials [12-17], such as aluminum, copper, carbon steel and stainless steel specimens, but the predictive equations for estimating erosion damage to SCR catalysts are limited. In lab-scale research, the catalyst samples are exposed to an accelerated abrasive environment to evaluate the total material loss [18,19]. However, due to the discrepancy between the experimental conditions in the laboratory and conditions in the field, the degree of erosion of a single catalyst sample cannot represent the erosion condition of the entire catalyst layer. Therefore, the environment in which catalysts operate must be simulated to establish an erosion model that represents a true SCR geometry.

CFD simulations have been extensively used in boiler design and optimization. Typically, CFD-based erosion simulations can be performed in three steps: flow modeling, particle tracking and erosion calculations [20]. Researchers [21-23] have focused on the modeling of both gas flow and NH3 mixing in full-sized SCR reactors for obtaining the velocity and concentration at the entrance of the catalyst layer. However, limited information is found in the literature on simulations of the particulate flow and catalyst erosion in industrial SCR systems. Xu et al. [24] established a three-dimen-

†To whom correspondence should be addressed.
E-mail: fqsi@seu.edu.cn
‡The paper will be reported in the 11th China-Korea Clean Energy Workshop.

sional CFD model for an SCR reactor to analyze the catalyst breakage failure; however, the results quantifying the erosion rate were not reported. Park et al. [25] studied the gas-solid flows and the erosion behavior inside the catalyst duct; however, they did not consider coupling the erosion model with a full-sized SCR reactor model.

In general, modeling catalyst erosion using CFD models presents a major problem. In practice, the catalyst layers inside an SCR reactor are composed of thousands of catalyst units with a certain geometrical structure, such as honeycomb monoliths or plates, and these structures can divide the boiler duct into numerous gas channels. In CFD models, the meshes must be large enough to exceed our current ability to computer generate an actual catalyst structure, because the mesh scale of a single catalyst plate and the scale of an entire SCR reactor are inconsistent. Therefore, certain simplifications must be performed. Researchers [8,22] have used a porous medium model to describe the catalyst layer and the inner region of the solid catalyst. However, porous medium models can only add viscous and inertial loss terms to the momentum equation and do not precisely convey the complex structure of the inner catalyst layer. Therefore, it is difficult to describe the collision process between ash particles and the real catalyst wall, which increases the difficulty of modeling catalyst erosion.

Our aim was to propose a new method of evaluating the erosion condition of commercial SCR catalysts in industrial boilers. In this method, a CFD-based approach is first introduced to describe the SCR reactor and calculate both the flue gas and fly ash distribution at the entrance of the catalyst layer. Then, a particle erosion model in the catalyst layer is established using MATLAB. In this model, a microhardness test is conducted for certain crucial modeling parameters. Relative cold state tests and erosion measurements are also conducted for numerical validation. Furthermore, the present study discusses the relationship between the catalyst erosion process and the SCR reactor installment, and a series of retrofit schemes are proposed.

EXPERIMENTS

This section introduces a series of experiments, including the cold state tests and relative erosion measurements, and these experimental results can be compared with the simulation results.

1. SCR System Description

Fig. 1 shows the general arrangement of the SCR DeNOx reactor for a 660 MW coal-fired boiler, which consists of fly ash hoppers, turning vanes, an ammonia injection grid (AIG), a set of straighteners, two catalyst layers, and groups of beam structures. Fig. 2 shows a schematic view of the catalyst arrangement. Each catalyst layer incorporates eighty catalyst modules arranged in ten columns in the Y-direction (eight modules per column), and each module is arranged with sixteen catalyst units filled with plate-type catalysts. Above the first catalyst layer, the steel #2 was installed to

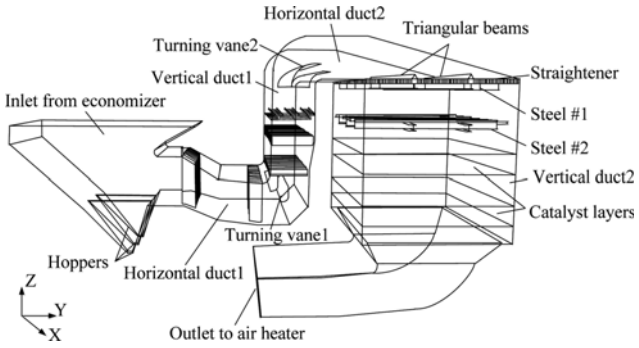

Fig. 1. General arrangement of the full-sized SCR reactor.

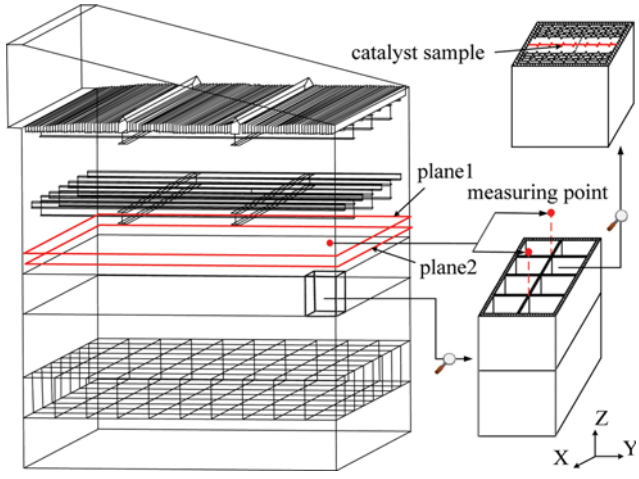

Fig. 2. Schematic of the catalyst samples and velocity measurement points.

support the spare catalyst layer, which is installed when the current 2-layer catalysts no longer operate efficiently. Under the straightener, the steel #1 is designed with the same structure as steel #2. A set of triangular beams is connected to the top of the straightener to prevent ash deposits on the surface of steel #1.

2. Cold State Test

To study the flow field at the entrance of the catalyst layer, a field test was performed in a cold state without furnace combustion in which the forced and induced draft fans were operated normally and all primary and secondary air registers maintained their usual openings. Fig. 2 shows that two velocity measuring points were assigned for each catalyst module at a distance of 0.7 m; thus, the total number of testing points was 180.

Moreover, to ensure that a similar flow distribution occurred between the cold-state test and the actual operational environment, we had to achieve geometric, kinematic and dynamic similarity. Because the test was operated in an actual unit and air density presents uniform characteristics, geometric and dynamic

Table 1. Calculation for a fully turbulent flow condition

Case	Material	Load (MW)	Temperature (°C)	Viscosity (kg/m·s)	Flow rate (m^3/s)	Velocity (m/s)	Reynolds number
Filed test	Air	0	20	1.82E-05	813	2.54	2.04E+06
BMCR	Flue gas	660	363	3.21E-05	1205	3.77	7.92E+05

Table 2. Detailed information of the catalyst sample

Period (mm)	Width (mm)	Pitch (mm)	Length (m)	Projected area (mm^2)	Designed life (h)	Operating hours (h)
12.5	1.8	6	0.57	264480	24000	15000

similarity can be easily satisfied. In addition, when the Reynolds number exceeds an approximate value of 100,000, kinematic similarity is achieved in a fully turbulent flow condition. Table 1 indicates that both the field test and actual operation of a full load occur in a fully turbulent region.

3. Erosion Measurement

To acquire the erosion condition of the SCR catalysts in the actual environment, a relative erosion measurement was performed during unit maintenance. As shown in Fig. 2, a total of 80 catalyst samples were collected from the 80 catalyst modules in the first catalyst layer. The erosion depth of each catalyst sample was quantitatively evaluated using Eq. (1), and the erosion degree, which was classified from 1 to 6, was defined to separately indicate the erosion depth in the range of 0 to 5 cm, 5 to 10 cm, 10 to 15 cm, 15 to 20 cm, 20 to 25 cm, and above 25 cm. Table 2 lists detailed information on the catalyst samples.

$$l_t = \frac{A_t}{A_{samp}} l_{samp} \quad t = 1, 2, \cdots, 80 \tag{1}$$

where l_t is the erosion depth of the catalyst sample, l_{samp} is the length of the catalyst sample, A_t is the eroded area of each catalyst sample according to a mesh measuring method, and A_{samp} is the original area of the catalyst sample.

The results of the erosion measurements are shown in Fig. 3. Two main phenomena can be observed. (1) The catalyst modules in the 2nd, 3rd, 6th and 7th columns suffered more erosion than their neighboring columns. (2) The most serious erosion region in the entire catalyst layer was located on the catalyst modules in the 2nd and 3rd columns.

MATHEMATICAL MODEL AND SIMULATION METHOD

To analyze the gas-solid flow behavior in the SCR reactor and predict the erosion condition of the catalysts, a numerical simulation was performed based on the following assumptions: (1) the SCR DeNOx system is under a steady-state condition; (2) the carrier gas is isothermal, and behaves as an incompressible Newtonian fluid; (3) the velocity distribution of the carrier gas in the economizer outlet is even; (4) the carrier gas in the catalyst layers is regarded as flow in a porous media; (5) the chemical reaction in the catalyst layers is negligible; (6) two-way coupling effects and particle-particle interactions are negligible; and (7) the influence of the AIG structure on flow field is negligible.

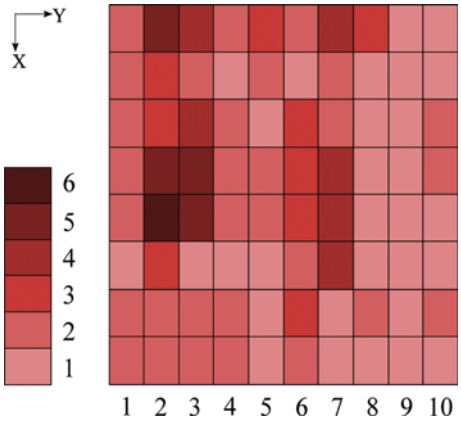

Fig. 3. Erosion distribution of the first catalyst layer.

Based on the above assumptions, this section presents four separate mathematical models for two phase motion (gas and dispersed phases), particle-wall collision and catalyst erosion, and then the simulation method is described.

1. Gas Phase Model

The mass and momentum conservation equations for the gas phase can be written as follows:

$$\frac{\partial}{\partial x_i}(\rho u_i) = 0 \tag{2}$$

$$\frac{\partial}{\partial x_j}(\rho u_i u_j) = -\frac{\partial p}{\partial x_i} + \frac{\partial}{\partial x_j}\left[\mu\left(\frac{\partial u_i}{\partial x_j} + \frac{\partial u_j}{\partial x_i}\right)\right] + S_i \tag{3}$$

The standard k-epsilon model is used to portray the turbulent flow in the following manner:

$$\frac{\partial}{\partial x_i}(\rho k u_i) = \frac{\partial}{\partial x_j}\left[\left(\mu + \frac{\mu_t}{\sigma_k}\right)\frac{\partial k}{\partial x_j}\right] + G_k + G_b - \rho\varepsilon - Y_M + S_k \tag{4}$$

$$\frac{\partial}{\partial x_i}(\rho \varepsilon u_i) = \frac{\partial}{\partial x_j}\left[\left(\mu + \frac{\mu_t}{\sigma_\varepsilon}\right)\frac{\partial \varepsilon}{\partial x_j}\right] + C_{1\varepsilon}\frac{\varepsilon}{k}(G_k + C_{3\varepsilon}G_b) - C_{2\varepsilon}\rho\frac{\varepsilon^2}{k} + S_\varepsilon \tag{5}$$

The eddy viscosity is calculated as follows:

$$\mu_t = \rho C_\mu \frac{k^2}{\varepsilon} \tag{6}$$

where, $C_{1\varepsilon}$, $C_{2\varepsilon}$, $C_{3\varepsilon}$, C_μ, σ_k, σ_ε are the model constants in Eqs. (4), (5), (6), and the values have been determined from various experiments [26].

As mentioned, the gas flow in the catalyst layers was treated as if it occurred in porous media. In the porous region, the momentum source consists of a viscous loss term and an inertial loss term, which can be described as Eq. (7) for the X, Y and Z directions.

$$\Delta P/L = K\mu u + C_2\frac{1}{2}\rho u^2 \tag{7}$$

In the X- and Y-directions (normal to the catalyst wall body), K and C_2 can be calculated using the Ergun semi-empirical formula [8]:

$$K = \frac{150(1-\gamma)^2}{D_P^2 \quad \gamma^3} \tag{8}$$

$$C_2 = \frac{3.5(1-\gamma)}{D_P \quad \gamma^3} \tag{9}$$

Table 3. Parameter values of the gas phase equations

Parameter	γ	D_P	K_x	C_{2x}	K_y	C_{2y}	K_z	C_{2z}
Value	0.423	1E-06	8.4E+14	3.95E+07	8.4E+14	3.95E+07	6.53E+05	5.71

In the Z-direction (parallel to the catalyst channel), K and C_2 can be calculated by fitting the operating data [22]. The relationship between the pressure loss of the two catalyst layers ΔP and the flow rate in the SCR reactor Q can be written as follows:

$$\Delta P=0.0002Q^2+0.3542Q \tag{10}$$

Table 3 lists the parameter values of the gas phase equations.

2. Dispersed Phase Model

The dispersed phase is based on a Lagrangian framework achieved by tracking all particle trajectories. The position and velocity of the particles can be calculated by solving the force balance equations:

$$m_p\frac{d\mathbf{u}_p}{dt}=\mathbf{F}_D+\mathbf{F}_G+\mathbf{F}_{LS} \tag{11}$$

$$\frac{d\mathbf{x}_p}{dt}=\mathbf{u}_p \tag{12}$$

The drag force can be calculated as follows:

$$\mathbf{F}_D=m_p\frac{18\mu}{\rho_P d_p^2}\frac{C_D Re_p}{24}(\mathbf{u}-\mathbf{u}_p) \tag{13}$$

$$Re_p=\frac{\rho d_p|\mathbf{u}_p-\mathbf{u}|}{\mu} \tag{14}$$

The drag coefficient can be determined as follows:

$$C_D=\begin{cases}\dfrac{24}{Re_p}(1+0.15Re_p^{0.687}) & Re_p\le 1000\\ 0.44 & Re_p>1000\end{cases} \tag{15}$$

The gravity and buoyancy can be written as follows:

$$\mathbf{F}_G=m_p\mathbf{g}\left(1-\frac{\rho}{\rho_P}\right) \tag{16}$$

Saffman's lift force can be calculated as follows:

$$\mathbf{F}_{LS}=m_p\frac{2K_{LS}\nu^{1/2}\rho d_{ij}}{\rho_P d_P(d_{lk}d_{kl})^{1/4}}(\mathbf{u}-\mathbf{u}_p) \tag{17}$$

where K_{LS}=2.594 and d_{ij} is the deformation tensor [27].

3. Particle-wall Collision Model

To obtain the trajectory of a particle impacting the wall surface in a boiler duct, an accurate particle-wall rebound model must be incorporated in the simulation. The coal-steel impact experiment conducted by Schade [12] demonstrates that the real particle impact angle was equal to the particle trajectory impact angle, with a wall roughness and particle shape correction according to the so-called shadow effect theory proposed by Sommerfeld and Huber [28]:

$$\alpha'=\max(1,\beta)\times\alpha \tag{18}$$

$$\beta=-2.202\times10^{-5}\alpha^3+1.837\times10^{-3}\alpha^2 -6.519\times10^{-2}\alpha+1.816+9.522\times10^{-8}\alpha^{-1} \tag{19}$$

With the assumption that the rotational velocity before impact is 0, the modified Matsumoto-Saito model based on the experiment conducted by Schade [12] is given as follows:

$$V_{t2}=E_tV_{t1} \tag{20}$$

$$V_{n2}=-E_nV_{n1} \tag{21}$$

$$E_t=\begin{cases}5/7 & \alpha'>\alpha_f\\ 1.0-\mu_d(1+E_n)|V_{n1}/V_{t1}| & \alpha'<\alpha_f\end{cases} \tag{22}$$

where, α is the particle trajectory impact angle, β is the wall roughness and particle shape correction, α' is the impact angle, E_n is the normal coefficient of restitution and has a value of 0.36, E_t is the parallel coefficient of restitution, μ_d is the constant dynamic friction coefficient and has a value of 0.3, and α_f is the angle of transition from sliding to non-sliding impact and has a value of 35.

4. Erosion Model

The erosion rate e_r (kg/kg) is defined as the mass of the eroded material related to the mass of the erodent material and it is calculated by Eq. (23):

$$e_r=\frac{e_f}{Q_p} \tag{23}$$

We calculated the erosion degree of the catalysts by accumulating the mass loss caused by the impactions between ash particles and the catalysts in a certain region, and it can be expressed by Eq. (24):

$$E_f=\sum_f Q_p e_r \tag{24}$$

The particle-catalyst erosion model is based on the framework provided by Oka et al. [13,14], which is a general erosion model for any impact conditions and for any type of material. The erosion equation is provided in Eqs. (25)-(29):

$$E(\alpha)=g(\alpha)E_{90} \tag{25}$$

$$g(\alpha)=(\sin\alpha)^{n1}(1+Hv(1-\sin\alpha))^{n2} \tag{26}$$

$$E_{90}=10^{-9}\times K_1(Hv)^{k1}\left(\frac{V_P}{V_{ref}}\right)^{k2}\left(\frac{d_P}{d_{ref}}\right)^{k3} \tag{27}$$

$$n_1=s_1(Hv)^{q_1},\ n_2=s_2(Hv)^{q_2},\ k_2=2.3(Hv)^{0.038} \tag{28}$$

$$e_r=\rho_w E(\alpha) \tag{29}$$

The parameter values for the equations above are listed in Table 4.

To obtain the Vickers hardness of the catalyst samples, microhardness tests were conducted under a load of 10 g, and the value of in Table 4 is the average value of five measurements. The test facility and the Vickers micro-indentation are shown in Fig. 4.

5. Simulation Method

The simulation approach can be implemented in two stages. First, a 3D model was established for a full-sized SCR reactor using the

Table 4. Parameter values for the Oka erosion model

Parameter	Hv	ρ_w	s_1	s_2	q_1	q_2	K_1	k_1	k_3	V_{ref}	D_{ref}
Value	0.002216	1500	0.71	2.4	0.14	−0.94	65	−0.12	0.19	104	326

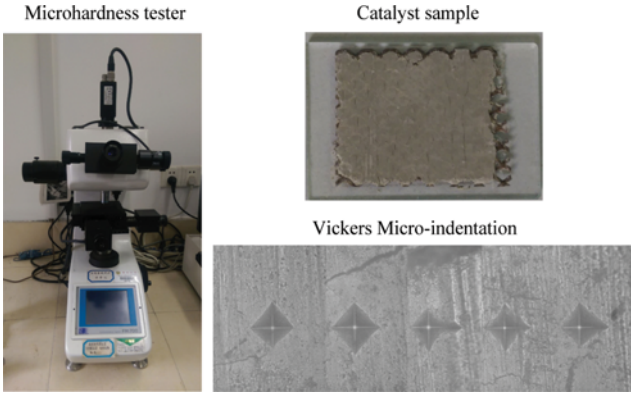

Fig. 4. Vickers hardness test of the catalyst sample.

commercial software FLUENT 14.5. The gas-solid flow was simulated based on the Eulerian-Lagrangian frame. The gas phase was regarded as a continuum, and the relative governing equation was solved using the SIMPLEC algorithm with pressure-velocity coupling. For the Lagrangian approach, each particle was tracked with a random initial position at the inlet profile, and the distribution of the particle diameter was divided into ten characteristic sizes from 2.5 μm to 300 μm according to the experimental data from Kuan et al. [29]. To further describe the flow behavior of large particles, the number of particles in each characteristic size group was equivalent, and the mass flow rate followed the Rosin-Rammler rule. The parameters for the initial and boundary conditions in the CFD model are listed in Tables 5 and 6, which show that the air mass flow rate and density were, respectively, 352.6 kg/s and 0.5491 kg/m^3, and the ash mass flow rate and density were respectively 10.56 kg/s and 1,000 kg/m^3; thus, the particle volume fraction and the solid-to-liquid ratios are, respectively, 1.65e-05 and 3%. In the present study, Kuan et al. [29] pointed out that one-way coupling models are used at which ash particle mass flow rate is below 7% of that of the flue gas, and Mezhericher [30] pointed out that the DPM approach gives satisfactory results at which the par-

Table 5. Boundary condition of the gas phase at the inlet and outlet profile

Case	Density (kg/m^3)	Viscosity (kg/(m·s))	Inlet		Outlet
			Velocity (m/s)	Temperature (K)	Pressure (Pa)
Cold state	1.1924	1.283e-05	3.4	293	0
Full load	0.5491	3.21e-05	4.65	636	0

Table 6. Boundary condition of the dispersed phase at the inlet profile

Case	Density (kg/m^3)	Temperature (K)	Velocity (m/s)	Total mass flow (kg/s)	Total number
Full load	1000	636	4.65	10.56	200,000

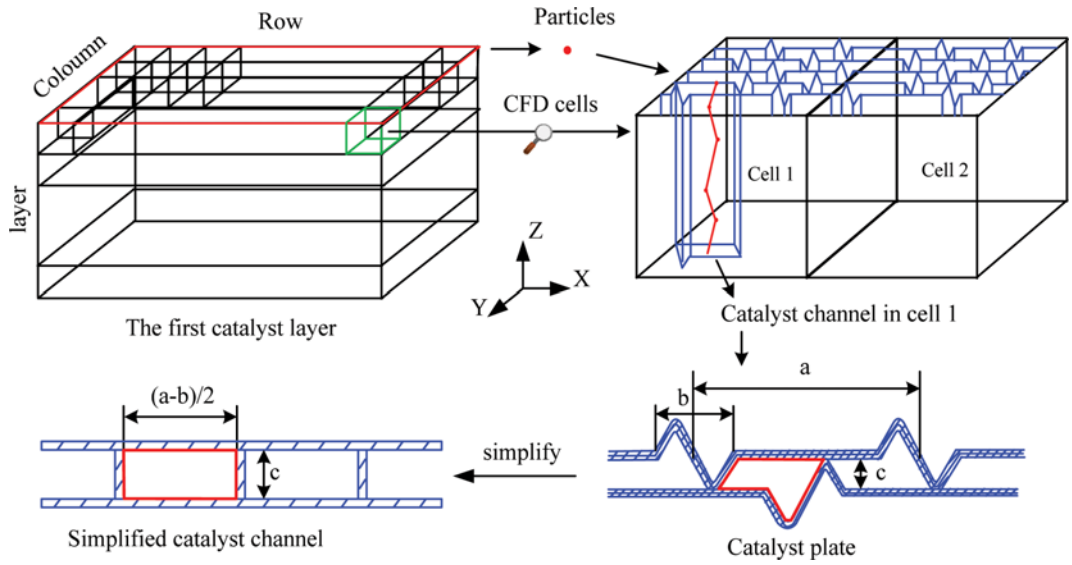

Fig. 5. Schematic of the MATLAB model (a=period; b=width; c=pitch).

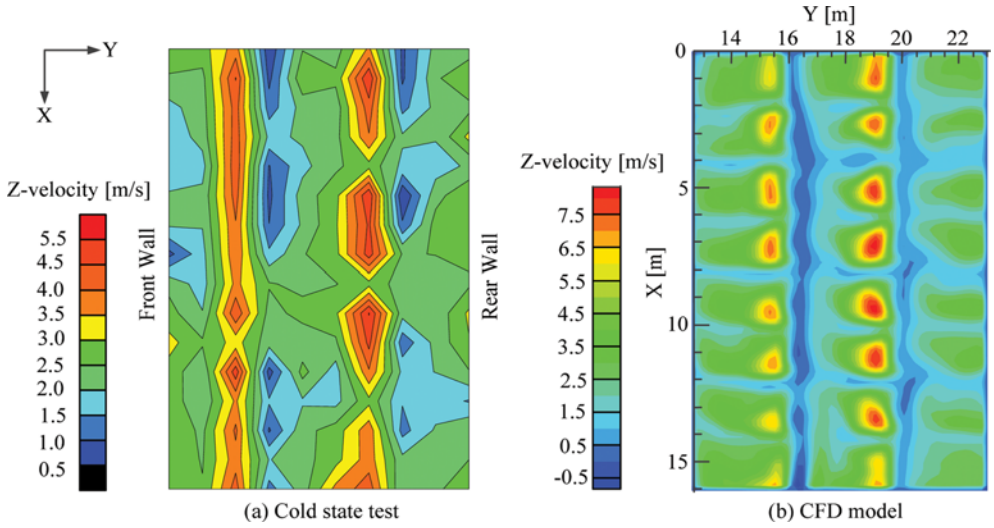

Fig. 6. Gas velocity nephograms on plane 1.

ticle volume fraction is below 0.1. Therefore, the two conditions in the references [29] and [30] were satisfied for our study, and the one-way coupling model DPM was used in our simulation. Furthermore, the user-defined function DEFINE_DPM_BC was developed to describe the particle-wall collision, and the fate of the particle was recorded as "trapped" when impacting the bottom surface of the ash hoppers; then, the trajectory calculations were terminated.

Second, due to the difficulty in calculating the collision and erosion process of the inner catalyst layer using the CFD model, a catalyst erosion model for each particle was established using MATLAB, and it was coupled with the results of the CFD model. A schematic of this method is shown in Fig. 5, and the detailed steps can be illustrated as follows: (1) read the information of each particle at the entrance of catalyst layer obtained from the results of CFD model, including the particulate position, velocity, diameter and mass flow rate; (2) describe the actual position of each catalyst plate using 3D MATLAB coordinates and assign a serial number to each catalyst channel; (3) determine the catalyst channels that contain each tracing particle; (4) determine the CFD cells that contain each tracing particle and obtain the local gas velocity; (5) calculate the drag force, Saffman lift force, gravity, buoyancy and acceleration of the tracing particle; (6) calculate the particulate position and velocity in the next time step; (7) determine whether particle-catalyst collision is occurring by comparing the spatial distance of the tracing particle and the catalyst walls; (8) if the collision occurs, calculate the erosion loss and update the particulate position and velocity in the next time step; (9) if not, go back to step (4) until the particles pass through the catalyst layer; and (10) perform these steps for each particle and accumulate the erosion loss in a different region.

RESULTS AND DISCUSSION

1. Validation of the Numerical Simulation

To validate the accuracy of the simulation results, a field test in a cold state was performed to measure the z-velocity on plane 1 (see Fig. 2), which was 0.7 m above the first catalyst layer. In the numerical simulation, case1 was conducted based on the original structure of the SCR reactor in which the cold-state air was regarded as the flow media to simulate the cold state environment; the modeling information is provided in Table 5.

Fig. 6(a) and Fig. 6(b) show the gas velocity nephograms from the cold-state test and the CFD model, respectively. The results are similar, and both cases have a relative uniform flow field along the X-direction except for the seven relative low velocity regions in the CFD calculation, which are directly below the seven I-shaped beams along the X-direction (see Fig. 2) and have no velocity test points. However, the velocity along the Y-direction from both the cold-state test and CFD results has a poor distribution, and two symmetrical regions have extremum velocity values. One region is the adjacent peak and valley velocity area on the two sides of the position at approximately Y=16 m, and the other region has a similar local velocity distribution on the two sides of the position at approximately Y=20 m. Fig. 7 shows that there is consistency between

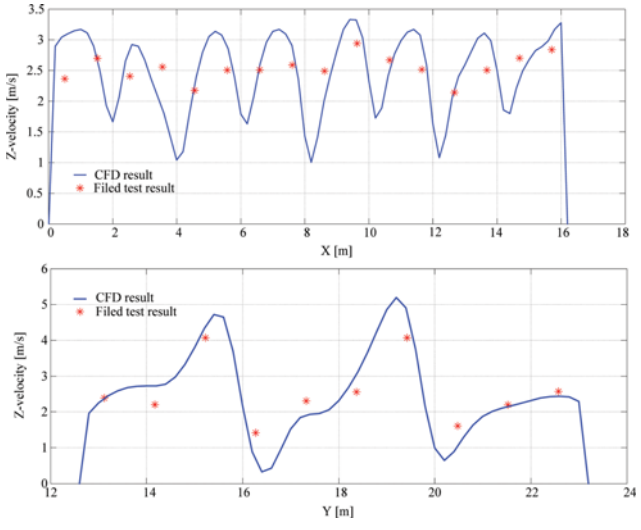

Fig. 7. Velocity distribution along the X- and Y-direction on plane 1.

Table 7. Information for case2, case3 and case4

Elements	Case2	Case3	Case4
Triangular beams	No	No	No
Support steel2	Yes	No	No
Support steel1	Yes	Yes	No

the results of the CFD model and the cold-state test, and both results demonstrate that there is an obvious bimodal velocity distribution along the Y-direction, and show that these distributions are directly above the catalyst modules in the third and seventh columns.

2. Effects of the Inner Structure Elements on the Gas Flow Field Distribution

As shown in Fig. 1, three inner structure elements, including triangular beams, steel #1 and steel #2, could affect the gas field distribution in contact with the catalyst layer. To investigate the respective influence of the three elements on the bimodal velocity distribution discussed above, three cases were designed and tested in a cold state. Case2, case3 and case4 are listed in Table 7. For example, case2 refers to removing off the triangular beams based on the original structure.

Fig. 8(a) through Fig. 8(d) show the velocity nephograms and streamlines from case1 through case4. Fig. 8(a) shows that when the flue gas turns into vertical duct2 (see Fig. 1), part of the gas flow contacts the surface of the two triangular beams and then changes direction before entering the straightener, which leads to the formation of the high velocity region along the windward side and the main vortex region along the leeward side. After passing through the straightener, steel #1 maintains the gas diversion effect by slowing the flow field recovery rate, whereas steel #2 generates a second vortex. Fig. 8(b) shows that the main and second vortex disappear via getting rid of the triangular beam. From Fig. 8(a) to Fig. 8(d), we can see that the high velocity region before entering the first catalyst layer gradually disappears, which illustrates that the beam groups close to the entrance of vertical duct2 and the first catalyst layer are primarily responsible for the formation of the bimodal velocity distribution.

3. Particle Trajectories and Distribution

To study the distribution and trajectories of the ash particles, case5 was designed to simulate the full load operation in which hot flue gas and fly ash particle served as the gas and solid flow medium. The detailed modeling parameters are shown in Table 5 and Table 6.

Fig. 9 and Fig. 10(a) show the velocity distribution of four types of particles at the entrance profile of the first catalyst layer in both the 3D and 2D views. The particles in four size groups that have similar velocity distributions with the gas phase, thus demonstrating good particle following behavior, and this velocity distribution is a bimodal distribution along the Y-direction. However, with an

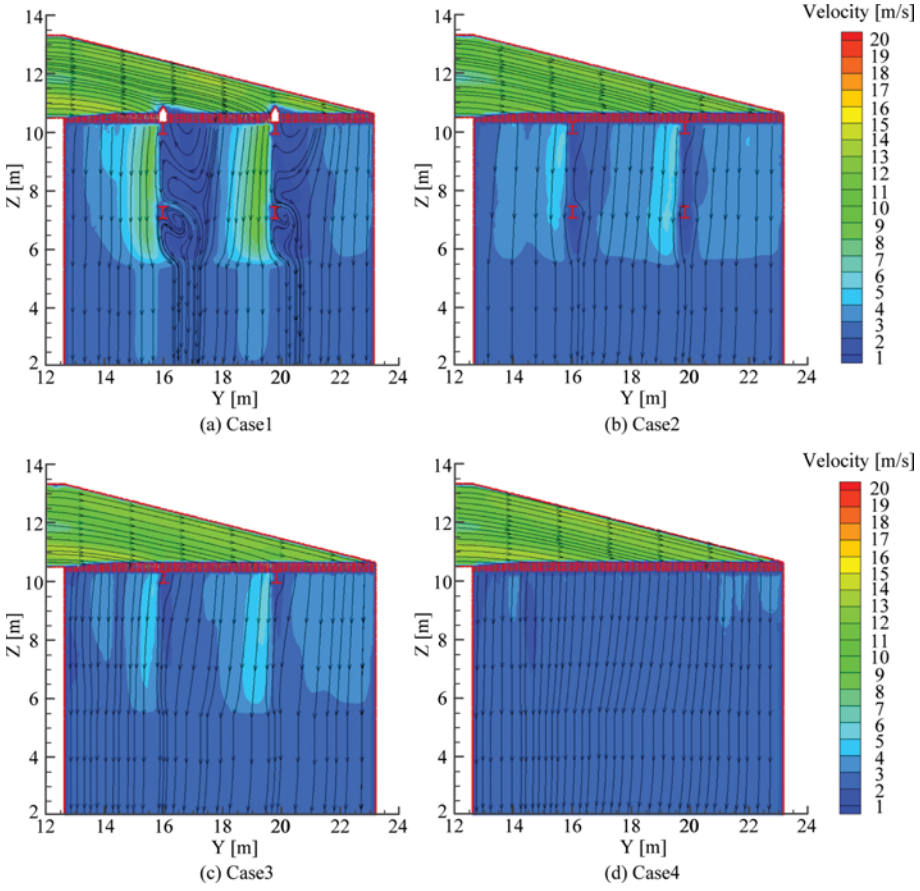

Fig. 8. Gas velocity streamlines in the YZ-plane at x=7 m from case1 through case4.

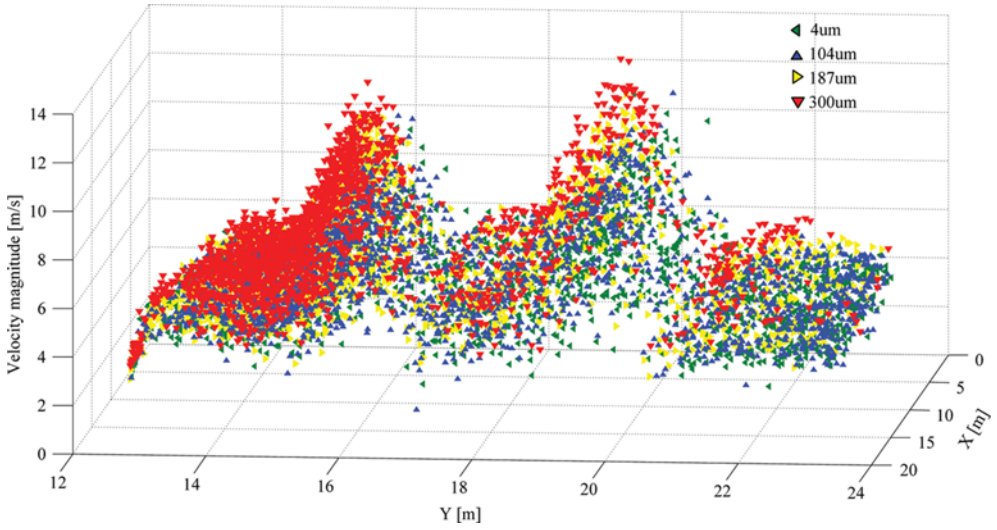

Fig. 9. Velocity distribution of the particles in the four size groups on plane 2 from case5.

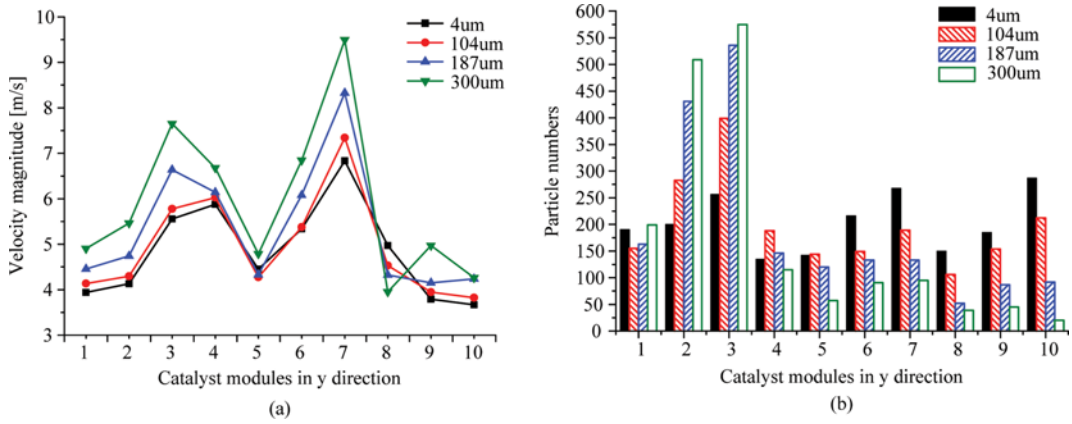

Fig. 10. Particulate velocity and numbers distribution in the Y-direction from case5.

increase in the particulate diameter, the particulate velocity increases because of gravity and inertia effects, which suggests that large particles, which maintain greater momentums, are more likely to separate from the flue gas. As shown in Fig. 10(b), most of the large particles are concentrated on the catalyst modules in the second and third columns. However, the distribution of smaller particles is relatively uniform, which reveals a strong correlation with the velocity distribution as indicated by the particulate numbers in the third and seventh catalyst columns, which are slightly greater than that of their neighboring columns. This result illustrates that the ash concentration of small particles is directly affected by the local flow field; beyond that, the upstream gas flow behavior and the installed elements also have a significant influence on the distribution of large ash particles.

The distribution of large particles is mainly attributed to the gas-solid flow through the two elbows before entering vertical duct2 (see Fig. 1). Fig. 11 shows the particulate trajectories in four size groups, and the ash particles from the economizer are influenced by gravity and drag force in the negative Z-direction. Compared with small ash particles (see Fig. 11(a)) which tend to maintain a well-dispersed distribution in the gas phase, large particles have greater inertia and can easily move towards the bottom wall of horizontal duct1, and the particles near the bottom wall cannot be deflected effectively in the two elbows because of the position of turning vane1 and turning vane2. Therefore, large ash particles are concentrated on one side of vertical duct1 and horizontal duct2 (see Fig. 1). Fig. 12(a) illustrates the flow field after turning vane2 and shows that it is nonuniform, which results in the reduced dispersal distribution of large particles and a greater portion of large particles falling into the catalyst modules in the second and third columns. Moreover, because of the separation effect caused by the triangular and I-shaped steel beams, extremum high and low velocity zones are formed in the windward and leeward side. These zones affect the particulate velocity and incident angle and influence the local distribution of the fly ash, especially for small particles, which explains why the particulate number in the third and seventh catalyst columns are slightly greater than that of their neighboring columns.

4. Erosion Analysis and Optimal Strategy

According to the analysis of the gas phase flow above, the beam

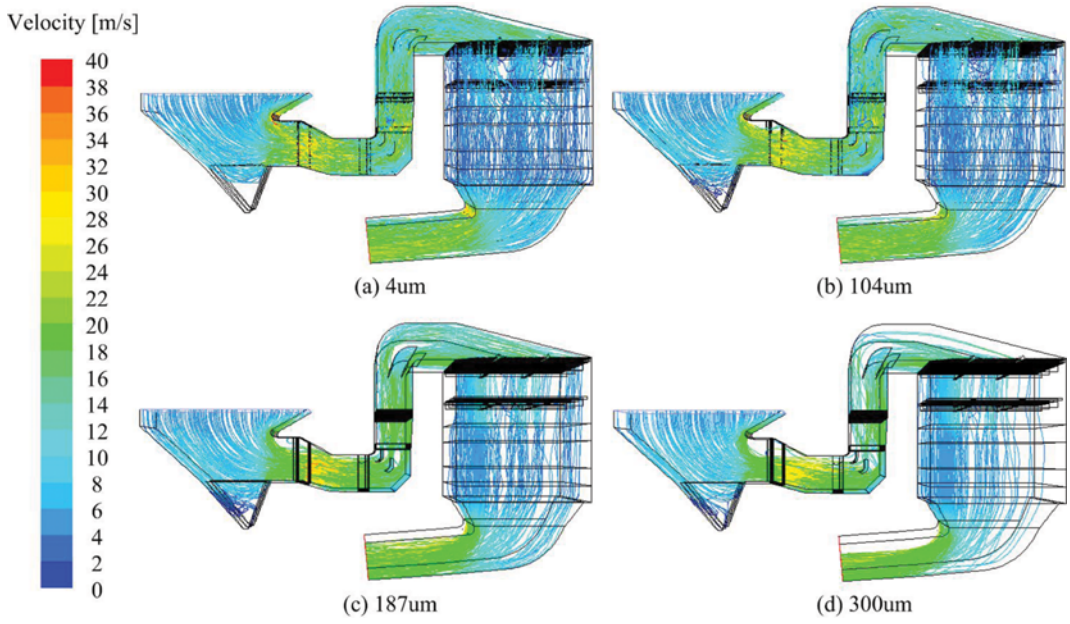

Fig. 11. Trajectories of the particles in the four size groups from case5.

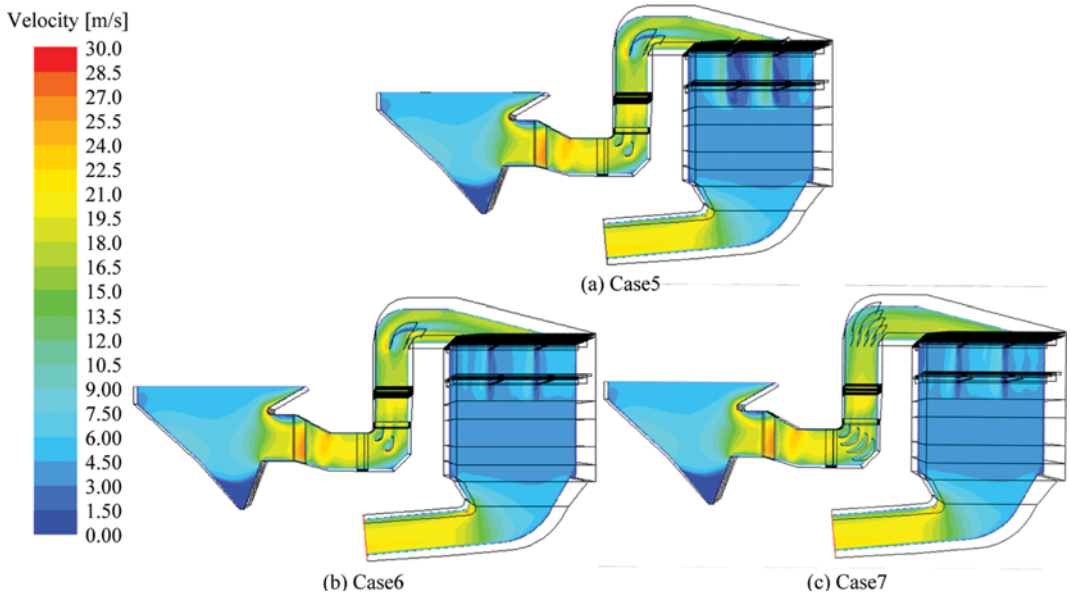

Fig. 12. Gas velocity distribution in the YZ-plane at x=7m from case5 through case7.

structures, which consist of a triangular beam, steel #1 and steel #2, would disturb the flow field before entering the first catalyst layer. Steel #1 and steel #2 were designed to support the load of the straightener and the spare catalyst layer, respectively, and they cannot be easily retrofitted, whereas the triangular beams were installed to prevent ash deposits on steel #1. Fig. 8 and Fig. 12 show that the gas velocity in horizontal duct2 is almost parallel to the upper surface of steel #1, and when using the retrofit scheme in case6, extreme low velocities do not occur in this region; thus, the chance of ash deposition is low. Therefore, case6 is developed to eliminate the triangular beams based on case5, and both the area and magnitude of the high velocity region at the entrance of the catalyst layer are obviously decreased, as shown in Fig. 12(a) and Fig. 12(b).

Fig. 13 shows the distribution of the particulate number on the Y-Z plane in which 200,000 particles, which are divided into ten equal groups, are calculated with the mass flow rate following the Rosin-Rammler rule. Fig. 13(a) and Fig. 13(b) show that the ash distribution before entering the vertical duct2 has no obvious change, whereas the area of high ash concentration above the seventh catalyst column decreases because of the effect of the flow field optimization in case6.

Case7 was performed to redesign the structure of turning vane1 and turning vane2 based on case6 for adjusting the ash distribu-

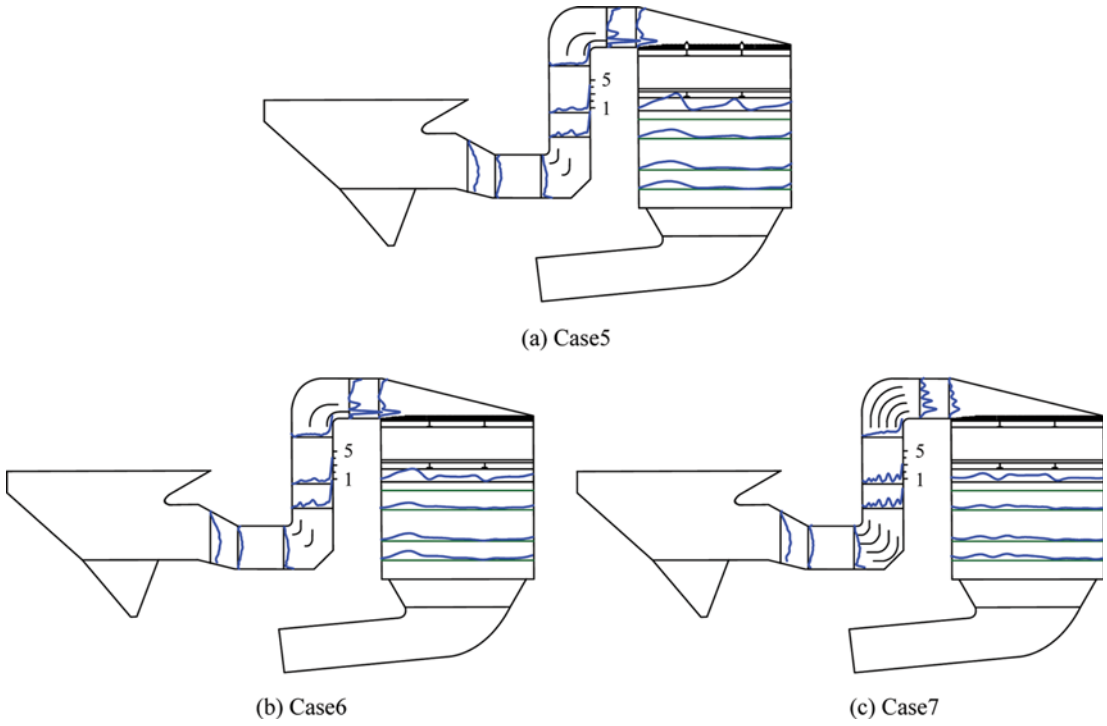

Fig. 13. Distribution of particulate number on the Y-Z plane from case5 through case7.

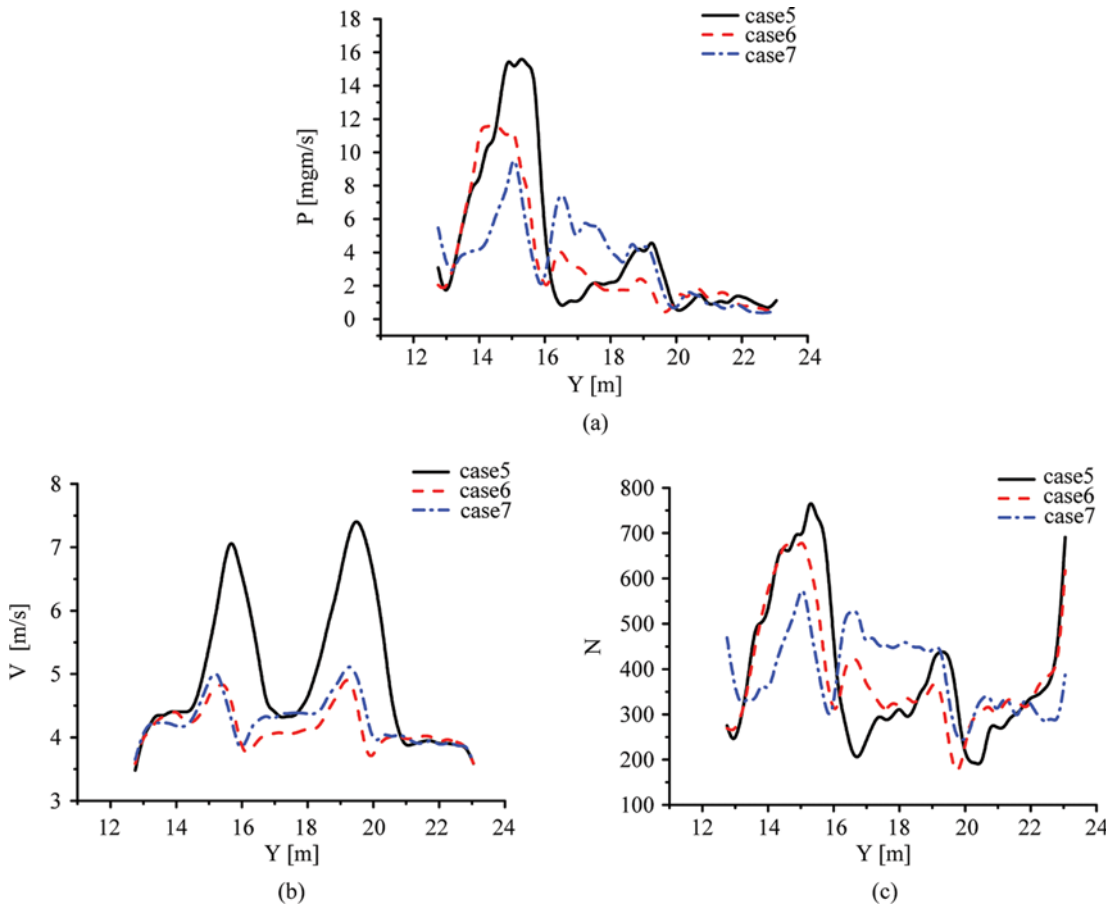

Fig. 14. Particulate velocity, number and carried momentum distribution along the Y-direction in plane2.

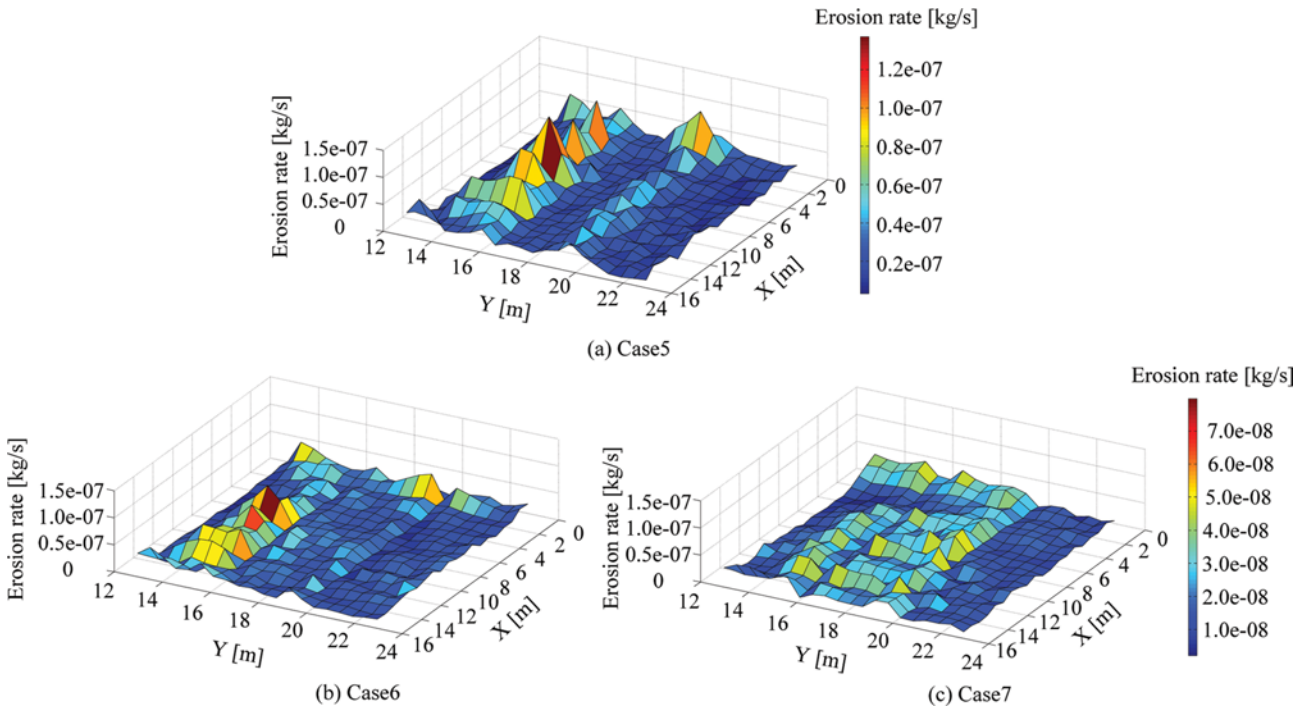

Fig. 15. Distribution of the catalyst erosion rate in the Y-Z plane from case5 through case7.

tion before vertical duct2 and the catalyst layer. As shown in Fig. 13(b) and Fig. 13(c), the number of turning vane1 has been increased to enhance the separation effect of the ash particles near the wall face of horizontal duct1 and reduce the ash non-uniformity before entering turning vane1. In addition, because the boiler duct was divided into several channels by turning vane1 and turning vane2, the import and export intervals of each channel were designed according to the flow distribution of the entering profile. Fig. 13(b) and Fig. 13(c) show that the flow distribution in horizontal duct1 becomes uniform after retrofitting the turning vanes, which also results in an improvement in the ash distribution before entering vertical duct2.

Fig. 14 shows the distribution of the particulate velocity, number and carried momentum along the Y-direction on plane2. Case6 is mainly designed to relieve the phenomena associated with the bimodal velocity distribution, and the major effect of case7 is to eliminate the local high ash concentration; thus, the distribution of particulate carried momentum also gradually improves. Furthermore, the catalyst erosion rate has been calculated based on the particulate velocity, diameter, mass flow rate and impact velocity and the material of the catalyst plate. Fig. 15 divides the catalyst layer into 400 regions in the X-Y direction, and the mass loss rate in each region has been calculated. The results of the numerical simulation (see Fig. 15(a)) are consistent with the conclusion of the erosion measurement (see Fig. 3), which indicated that the erosion rate of the catalyst layer is also a bimodal distribution that is similar to the velocity distribution. However, although the velocity near Y=20 m is slightly greater than the velocity near Y=16 m, the position of the greatest ash flow rate is near Y=16 m, which results in the maximum erosion rate in this area. Fig. 15(b) and Fig. 15(c) show that the retrofit scheme in case6 plays a major role in achieving a uniform erosion distribution because of the flow field optimization, whereas the optimized effect has been further improved through the ash field optimization in case7.

CONCLUSIONS

A combined gas-solid flow and catalyst erosion model was established for an industrial SCR DeNOx reactor in which the model parameters for the eroded material were obtained from a microhardness test. The simulation results are consistent with the relative cold state test results and the erosion measurements, thus indicating the potential of the model for predicting the catalyst erosion rate, and evaluating the position at which severe erosion is more likely to occur.

The coupled model is also a powerful tool for erosion optimization. Catalyst erosion was greatly influenced by the working environment, namely, the gas and ash flow field. However, the velocity uniformity in front of the catalyst layer is mainly attributed to local components, such as the beam groups close to vertical duct2 and the catalyst layer. The ash distribution is related to the components as well as the entire flow path, especially for the turning vanes in the elbows, where there is poorer flow behavior due to the inertia effect.

The retrofit scheme was implemented in an actual engineering application as an integrated method that includes numerical simulations and a relative experiment. Moreover, this model can be used for catalyst erosion predictions and is suitable for different types of catalysts and industrial SCR DeNOx systems.

ACKNOWLEDGEMENTS

This study was supported by the China Datang Corporation and

the Technology Support Program of Nanjing City.

NOMENCLATURE

Alphabetical Symbols

C_D : drag coefficient
C_2 : inertial resistance coefficient
D_p : mean particle size of the catalysts [m]
d_p : particle diameter [m]
d_{ref} : the reference particle diameter [m]
E_f : mass erosion rate of a material in a certain region [kg/s]
E_n : the normal coefficient of restitution
E_t : the parallel coefficient of restitution
$E(\alpha)$: erosion damage at an impact angle α [m^3/kg]
E_{90} : erosion damage at normal impact angle [m^3/kg]
e_f : mass erosion rate of a material by single particle [kg/s]
e_r : the mass of the eroded material related to the mass of the erodent material [kg/kg]
$\mathbf{F}_D$: drag force [N]
$\mathbf{F}_G$: gravity and buoyancy [N]
$\mathbf{F}_{LS}$: Saffman lift force [N]
G_k : the generation of turbulence kinetic energy due to the velocity gradients [kg/(m·s^3)]
G_b : the generation of turbulence kinetic energy due to buoyancy [kg/(m·s^3)]
$\mathbf{g}$: the acceleration of gravity [m/s^2]
Hv : vickers number [GPa]
K : viscous resistance coefficient
k : turbulence kinetic energy [m^2/s^2]
L : thickness of the porous media region [m]
m_p : particle mass [kg]
p : pressure [Pa]
Δp : total pressure loss of the two catalyst layers [Pa]
Q : flow rate in the SCR reactor [m^3/s]
Q_p : mass flow rate of a single particle that collides with the target face [kg/s]
Re : Reynolds number
Re_p : particle Reynolds number
S_i : momentum source term [N/m^3]
S_k : turbulence kinetic energy source term [kg/(m·s^3)]
S_ε : turbulence dissipation rate source term [kg/(m·s^4)]
$\mathbf{u}$: gas velocity [m/s]
$\mathbf{u}_p$: particle velocity [m/s]
u_i : the gas velocity in i-direction [m/s]
V_{t1} : impact velocity in the tangential direction [m/s]
V_{t2} : rebound velocity in the tangential direction [m/s]
V_{n1} : impact velocity in the normal direction [m/s]
V_{n2} : rebound velocity in the normal direction [m/s]
V_{ref} : the reference impact velocity [m/s]
$\mathbf{x}_p$: particle position [m]
x_i : the coordinate in i-direction [m] (if i=1 x, if i=2 y, if i=3 z)
Y_M : the contribution of the fluctuating dilatation in compressible turbulence to the overall dissipation rate [kg/(m·s^3)]

Greek Symbols

α : the particle trajectory impact angle [°]
α' : the impact angle [°]
α_f : the angle of transition from sliding to non-sliding impact [°]
β : the wall roughness and particle shape correction coefficient
γ : porosity of the catalysts [m^2/s^3]
σ_k : turbulent Prandtl number for k
σ_ε : turbulent Prandtl number for e
ε : turbulence dissipation rate [m^2/s^3]
μ : gas molecular viscosity [kg/(m·s)]
μ_d : the constant dynamic friction coefficient
ρ : gas density [kg/m^3]
ρ_p : particle density [kg/m^3]
ρ_w : catalyst density [kg/m^3]

Subscripts

p : ash particle
w : catalyst wall
ref : reference condition
t : wall tangent
n : wall normal

REFERENCES

1. P. Forzatti, *Appl. Catal. A: Gen.*, **222**, 221 (2001).
2. K. V. Shah, M. K. Cieplik, C. I. Betrand, W. L. van de Kamp and H. B. Vuthaluru, *Fuel Process.Technol.*, **91**, 531 (2010).
3. S. A. Benson, J. D. Laumb, C. R. Crocker and J. H. Pavlish, *Fuel Process. Technol.*, **86**, 577 (2005).
4. J. R. Strege, C. J. Zygarlicke, B. C. Folkedahl and D. P. McCollor, *Fuel*, **87**, 1341 (2008).
5. C. H. Bartholomew, *Appl. Catal. A: Gen.*, **212**, 17 (2001).
6. Z. Lei, C. Wen, J. Zhang and B. Chen, *Ind. Eng. Chem. Res.*, **50**, 5942 (2011).
7. T. Schwämmle, F. Bertsche, A. Hartung, J. Brandenstein, B. Heidel and G. Scheffknecht, *Chem. Eng. J.*, **222**, 274 (2013).
8. J. Yao, Z. Zhong and L. Zhu, *Chem. Eng. Technol.*, **38**, 283 (2015).
9. J. Yang, H. Ma, Y. Yamamoto, J. Yu, G. Xu, Z. Zhang and Y. Suzuki, *Chem. Eng. J.*, **230**, 513 (2013).
10. M. B. Gandhi, R. Vuthaluru, H. Vuthaluru, D. French and K. Shah, *Appl. Therm. Eng.*, **42**, 90 (2012).
11. G. C. Pereira, F. J. de Souza and D. A. de Moro Martins, *Powder Technol.*, **261**, 105 (2014).
12. K. P. Schade, H. J. Erdmann, T. Hädrich, H. Schneider, T. Frank and K. Bernert, *Powder Technol.*, **125**, 242 (2002).
13. Y. I. Oka, K. Okamura and T. Yoshida, *Wear*, **259**, 95 (2005).
14. Y. I. Oka and T. Yoshida, *Wear*, **259**, 102 (2005).
15. R. Nagarajan, B. Ambedkar, S. Gowrisankar and S. Somasundaram, *Wear*, **267**, 122 (2009).
16. Z. Lin, X. Ruan, Z. Zhu and X. Fu, *Powder Technol.*, **254**, 150 (2014).
17. Mansouri, H. Arabnejad, S. A. Shirazi and B. S. McLaury, *Wear*, **332**, 1090 (2015).
18. K. G. Budinski, *Wear*, **203**, 302 (1997).
19. L. Gan, S. Lei, J. Yu, H. Ma, Y. Yamamoto, Y. Suzuki and Z. Zhang, *Front. Environ. Sci. Eng.*, **9**, 979 (2015).
20. M. Parsi, K. Najmi, F. Najafifard, S. Hassani, B. S. McLaury and S. A. Shirazi, *J. Nat. Gas Sci. Eng.*, **21**, 850 (2014).
21. H. J. Chae, S. T. Choo, H. Choi, I. S. Nam, H. S. Yang and S. L.

Song, *Ind. Eng. Chem. Res.*, **39**, 1159 (2000).
22. J. M. Cho, J. W. Choi, S. H. Hong, K. C. Kim, J. H. Na and J. Y. Lee, *Korean J. Chem. Eng.*, **23**, 43 (2006).
23. Y. Xu, Y. Zhang, J. Wang and J. Yuan, *Comput. Chem. Eng.*, **49**, 50 (2013).
24. Y. Xu, Y. Zhang, F. Liu, W. Shi and J. Yuan, *Comput. Chem. Eng.*, **69**, 119 (2014).
25. H. C. Park, H. S. Choi and Y. S. Choi, *J. Comput. Fluids Eng.*, **16**, 66 (2011).
26. B. E. Launder and D. B. Spalding, *Comput. Methods Appl. Mech. Eng.*, **3**, 269 (1974).
27. A. Li and G. Ahmadi, *Aerosol. Sci. Technol.*, **16**, 209 (1992).
28. M. Sommerfeld and N. Huber, *Int. J. Multiphase Flow*, **25**, 1457 (1999).
29. B. Kuan, N. Rea and M. P.Schwarz, *Powder Technol.*, **179**, 65 (2007).
30. M. Mezhericher, T. Brosh and A. Levy, *Particul. Sci. Technol.*, **29**, 197 (2011).